Research Square

Preprints are preliminary reports that have not undergone peer review.
They should not be considered conclusive, used to inform clinical practice,
or referenced by the media as validated information.

Context Aware Fusion for Brain Disease Detection via Hybrid Decomposition and Optimization

SURANJANA MUKHERJEE

mala35b@gmail.com

Jadavpur University Faculty of Engineering and Technology

Sriparna Banerjee

Jadavpur University Faculty of Engineering and Technology

Sheli Sinha Chaudhuri

Jadavpur University Faculty of Engineering and Technology

Khalifa Djemal

Evry-Val-d'Essonne University: Universite d'Evry-Val-d'Essonne

Research Article

Keywords: multimodal imaging, image fusion, fusion rule, cardinal-subcardinal decomposition, moving average convergence-divergence filtering, gray wolf-world cup optimizer

Posted Date: March 31st, 2026

DOI: https://doi.org/10.21203/rs.3.rs-8732811/v1

License: This work is licensed under a Creative Commons Attribution 4.0 International License.
Read Full License

Context Aware Fusion for Brain Disease Detection via Hybrid Decomposition and Optimization

Suranjana Mukherjee[a,1], Sriparna Banerjee[b,1], Sheli Sinha Chaudhuri[c,1], Khalifa Djemal[d,2]

[1]Dept. of Electronics and Telecommunication Engineering, Jadavpur University, Kolkata, India
[2] *University of Évry Val d' Essonne, Paris, France*
[a]mala35b@gmail.com , [b]sriparnatinni@yahoo.in , [c]shelism@rediffmail.com, [d]Khalifa.Djemal@univ-evry.fr

*Corresponding Author: [a]mala35b@gmail.com

Abstract— *background-* **Integrating complementary information from multimodal images into single fused image is crucial for early and accurate diagnosis.** *Method-* **An innovative fusion framework is featuring Cardinal Sub-cardinal Directional Associated Filtering (CSDAF) to decompose input image (I) into Gross Layer (GL) and Residual Layer (RL) while another Fine Layer (FL) extraction is from I by applying a unique *Moving Average Convergence Divergence (MACD)* filtering technique. Dual activity measurement strategy is performed by a *twin channel Siamese Convolutional Neural Network (SCNN)* and *Self-Adaptive Pulsed Coupled Neural System (SAPCNS)* to generate a combined Activity Map of *Gross Layers (AM_{GL})* and *Fine Layers (AM_{FL})* respectively while AM_{GL} is undergone through multi-scale decomposition for context-aware fusion to obtain *Fused Gross Layer (GL_{FUSED})* by bi-decision rule based on *Similarity Measuring Coefficient (SMC)* and a parametric threshold (τ) obtained through a novel hybridization of *World Cup (WC)-Grey Wolf Optimization (GWO)* algorithms whereas Fused Residual Layer (RL_{FUSED}) is derived via *Cloud Coefficient (CC)* through a *Statistical Cloud Model (SCM)*.** *Results-***Experimental results on standardized benchmark databases demonstrate the superior performance of the proposed algorithm over existing methods, both qualitatively and quantitatively. It is observed that information integration (EN), clarity (SD and TMQI), edge quality (AG), activity level (SF) and simultaneous visualization (NMI), achieving up to a *10.5422%, 11.3300411%, 25.578%, 36.95%, 10.4448%, 2.0496% increases* in terms of *Entropy (EN), Standard Deviation (SD), Average Gradient (AG), Spatial Frequency (SF), Normalized Mutual Information (NMI)* and *Tone Mapped Quality Index (TMQI)* is improved in the proposed method with respect to the compared state-of-the-art techniques.** *Conclusion-* **The proposed image fusion algorithm has been shown to effectively preserve intricate details without compromising clarity, activity level preservation as evidenced by comprehensive qualitative and quantitative evaluations which may offer significant advantages in disease analysis, precise therapy and in broader image processing applications.**

Keywords: multimodal imaging, image fusion, fusion rule, cardinal-subcardinal decomposition, moving average convergence-divergence filtering, gray wolf-world cup optimizer

1. Introduction

With the advent of smart health care monitoring systems, the precise identification of the diseased *Region of Interest (ROI)* from non-invasive imaging data has become increasingly vital, as it helps in early disease detection and treatment planning in these scenario, medical image fusion is also effective in early diagnosis by providing composite information in a single image and also diminishes the storage cost of preserving multiple images. Complementary information are obtained by multi-modal imaging procedures, such as Single Photon Emission Computed Tomography with injection radio-active perfusion agent Tc99m (SPECT-Tc), Single Photon Emission Tomography with thallium-201 (SPECT-T1), Positron Emitted with Fluro-Deoxy-Glucose (PET-FDG) typically provide relevant functional information related to blood flow, food activity and metabolism of the affected region whereas Magnetic Resonance Imaging with weighted-T1 (MRI-T1), weighted-T2 (MRI-T2), and gradient (MRI-GAD) (Johnson, 2001) typically offer comprehensive anatomical information about affected soft tissue regions.

Fusion algorithms aim for being effective in clinical trials by retaining interrelated contextual information and spatial features from multiple images into a consolidated image. The fusion algorithms are categorized broadly as multiscale-transform (MST) approaches, neural network based and various types of edge-preserving-filtering (Basu et al. 2024, Bhosekar et al. 2024, Choudhary et al. 2023, Ghandour et al. 2024). The MST-based decomposition methods split the image matrix into one *Low Frequency Component (LFC)* containing gross information and many *multi-directional High Frequency Components (HFC)* consisting edge/textural details followed by the application of fusion rules on the generated sub-images to combine the multimodal information. Among various *MST*, *Non-subsampled Shearlet Transformation (NSST)* are mostly preferent by the researchers due to its multi-scale-spatial directional information extraction ability which can improve the fidelity of the image to some extent (Yin et al 2018, Tan et al 2020, Mukherjee et al 2020, Mukherjee et al 2021, Mukherjee et

al 2021, Sharma et al 2024, Qi et al. 2025). Few examples of NSST based approaches are regional energy conservation along with sparse representation and grey level co-occurrence adaptive PCNN (Qi et al. 2025), parametrically adaptive PCNN with spatial energy preservation (Yin et al 2018) parametrically optimized PCNN (Mukherjee et al. 2021), intrinsic mean energy attributed with boundary measured PCNN (Tan et al. 2020), Principal Component Analysis (PCA) based weighted averaging technique for appropriate assimilation of the regional properties of LFCs-HFCs after the vague set segmentation (Mukherjee et al. 2020) , related global optima measuring weighted averaging fusion by Particle Swam Optimization (PSO) (Mukherjee et al. 2021), max-entropy of squared coefficient based fusion rule and regional energy measuring technique (Sharma et al 2024).

The salient spatial edge representation approaches have especially acquired attention because of their increased computational efficiency owing to lesser number of sub-images extraction that results in achieving better luminance in the fused images. Few illustrations are extended difference of Gaussian estimation (Jie et al. 2023), capturing correlated features by coupled filters in convolutional dictionaries (Veshki et al. 2022), local extreme map guided filtering (Zhang et al. 2022), truncated Huber-filtering based decomposition with multiple-dictionary learning decisions and nuclear energy associated mechanism (Jie et al. 2024).

Deep learning networks have earned significant attention by the researchers in various field of image processing because they construct high level features by learning low level features (Sun al. 2024). Hence deep learning-based techniques have diversified application in segmentation (Guerroudji et al. 2024), image retrievals (Li et al. 2024), high-to-low-level feature matching and complementary information fusion for reference-based image super-resolution (Wang et al. 2024) and many more (Xia et al. 2024, Su et al. 2025, Jeong et al. 2025, Ince et al. 2025). It is also explored widely by the researchers in developing fusion methodologies, very few of them are reported in (Mukherjee et al. 2025, Li et al. 2022, Fan et al. 2025, Zhang et al. 2024, Pathak et al. 2026).

Few recent instances of deep learning fusion methodologies are dual-branch Siamese CNN (DSCNN) with simultaneous pixel level activity integration is utilized and edge preserving statistical property associated with SOLGWO (Mukherjee et al. 2025), significant feature extraction for fusion by CNN based dual branch residual attention module by (Li et al. 2022), lightweight medical image fusion network based on discrete wavelet convolution and selective state space models developed by (Fan et al. 2025) by acquiring a pair feature difference guided learning. Similar feature-based learning concepts are adapted in designing Triple disentangled dual attention network (Zhang et al. 2024), A lightweight medical image fusion network based on discrete wavelet convolution and selective state space models (Fan et al. 2025), optimal feature selection for medical image fusion using deep learning with transformer (Pathak et al. 2026) to reduce redundant features selection capacity.

Few instances of nature inspired soft computing methodologies like enhanced decomposition scheme with Chameleon Swarm (ChS) algorithm (Dinh 2023), homomorphic fusion scheme (Xu et al. 2020) by hybridizing Shark Smelling Optimization (SSO) with WCO and in (Mukherjee et al. 2025) GWO-soccer league optimization is used for image enhancement by scaling the sublayer imaged according to their information content which has played a significant role in the whole process of multimodal medical fusion.

The *GWO* and *WC* algorithms are preferred in this work for estimating the *parametric threshold (τ)* for combining sublayer images because of their improved capacity of finding global optima. In most of the bio-inspired approaches like particle swarm optimization, genetic algorithm, ChS, SSO and many more global optima finding is performed by one leader where as in *GWO* and *WC* stepwise local optimum finding strategy is adopted with three hierarchical leaders which enhances the convergence speed to reach the global optimum by leveraging continuous reduction in search that reduces the probability of getting stuck at the local optima and also guarantees faster convergence and faster convergence is also guarantees.

1.1 Contribution to address existing challenges and research gap

In spite of the presence of several fusion schemes, there stills exists significant research gaps and specific challenges which are highlighted as follows:

a) Fused images often suffer from misalignment, spectral distortion, and noise inclusion due to inappropriate color plane choosing and extraction of a large number of sub-images especially in MST-based methods, owing to deeper decomposition levels and complex decomposition-reconstruction procedures. To address this

limitation, the proposed method employs a novel and simple decomposition strategy, where *CSDAF* filtering technique is adapted by considering cardinal and sub-cardinal directional matrices to discriminate gross structural information which is referred as *GL* and similar as *LFC* in *MST* in another side composite directional textures are contained in *RL* and *FL by MACD* that are equivalent to *HFCs*; GL_{FUSED}, RL_{FUSED} and FL_{FUSED} are combined by pixel-level summation for reconstruction. The textural variations of I is captured in *FL* by *MACD*. The convergence in *MACD* means two underlying moving averages of pixel intensities are similar and moving towards each other because of having identical value while divergence means they are drifting apart. To the best of our knowledge this type of sublayer acquisition is adopted for the first time.

b) Proper acquisition of exact color and edge detailing with simultaneous visualization of multi-modal information in the fused image is still challenging. Addressing this issue, the proposed method presents a unique context-aware fusion rule for GLs with integration of max-rule and weighted combined activity mapping at multiscale resolution inclusive of determining image property-based threshold verification by proposing *a novel hybridization of WC and GWO where the scoring strategy of teams in WC is acting as fitness function in GWO*. The proposed hybridization technique also adapts Mantegna's algorithm during the position update to predict the random walks by the grey wolves.

c) The fusion rule is designed by leveraging dual Activity Level Measurement through deep learning based *dual channel SCNN* and *SAPCNS* for merging sub-layer images along with statistical property-based cloud model in hybrid decomposition domain, enhances the chance of better information incorporation without compromising clarity, activity level with enabling simultaneous perceptual visualization of complementary information.

The remaining portion of the article is organized as Methodology, Experimental Results, Conclusion in Section 2, 3 and 4 correspondingly.

2. Methodology

The fundamental contribution of the proposed work lies in integrating complementary information seamlessly in a fused image to derive the clinical decisions in a timely manner. The process begins with the conversion of functional information of PET/SPECT images from RGB to YUV and anatomical information of MRI to gray-scale for better preservation of colour saliency and information content. The whole process of fusion is solely designed by adapting the image-context based static properties. The proposed fusion scheme can be described briefly in the following steps: -

a) Decompose I_A and I_B into three sublayers (GL_A, RL_A, FL_A) and (GL_B, RL_B, FL_B) respectively by imposing the proposed *CSDAF* decomposition technique.

b) For dual strategic activity measurement, the combined AM_{GL} (of GL_A and GL_B) and AM_{FL} (of FL_A and FL_B) and are generated by the *twin branched SCNN and SAPCNS* correspondingly which enhances the chance of incorporating significant textural as well as gross information.

c) Decompose GL_A and GL_B by Laplacian pyramid and AM_{GL} through Gaussian pyramid to procure obscure pixel to pixel detailing and apply the proposed fusion rule to obtain *Fused Gross Layer* (GL_{FUSED}).

d) Derive the respective *Statistical Cloud Coefficients* (SCC_A *and* SCC_B) from the *SCM* and impose the proposed fusion rule to obtain *Fused Residual Layer* (RL_{FUSED}) comprising of every relevant property from neighborhood in accordance with current pixel location.

e) *Fused Fine Layer* (FL_{FUSED}) is obtained on the basis of their pixel level activities-based decision mapping by AM_{FL}.

f) Amalgamate *fused Y-plane* (Y_{FUSED}) by pixel level summation of GL_{FUSED}, RL_{FUSED} and FL_{FUSED}.

g) Successively merge Y_{FUSED} with U and V followed by YUV to RGB color plane conversion to obtain the final fused image.

The pictorial representation of the entire proposed fusion scheme is illustrated in Fig.1.

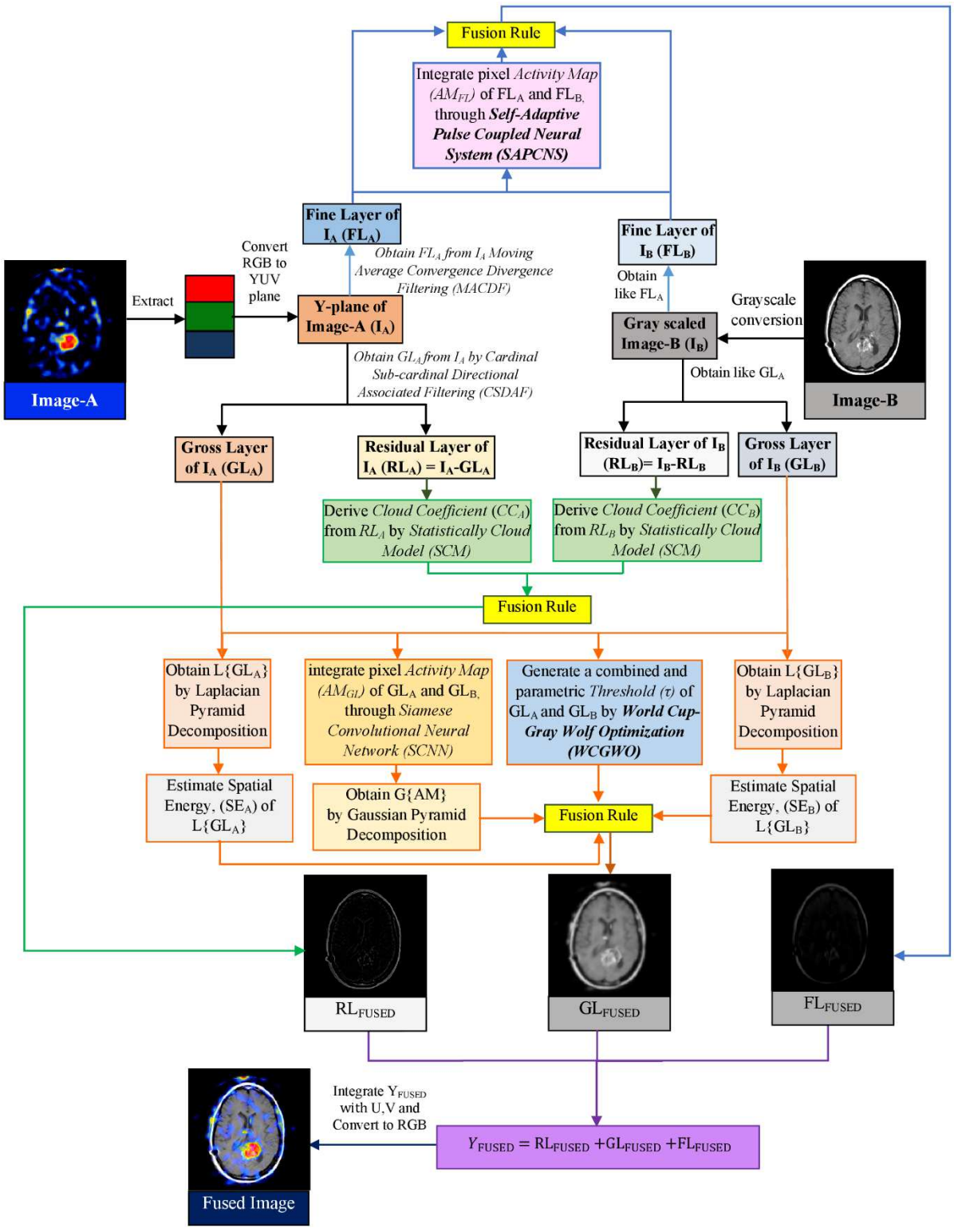


Fig.1: Schematic view of the proposed fusion scheme

Detailed discussion on each step adopted in the proposed scheme is described in the following subsections.

2.1. Cardinal Sub-cardinal Associated Filtering based decomposition

The present study proposes *CSDAF* type decomposition process where it is acting as a smoothing filter to estimate GL through convolving I_A/I_B with the cardinal and sub-cardinal directional matrices. This decomposition process is proposed and imposed to extract only two sublayers (GL and RL) of an image to prevent loss of information and save overall computation time as only two sub-images are derived. All

significant structural information is contained in the estimated *GL* while the *RL* contains to edges, contours, texture and intensity variations etc. The decomposition of Y-component of I_A into GL_A, RL_A and I_B into GL_B, RL_B is conducted using Algorithm 1.

Algorithm1: Two Scale Image Decomposition

Input: Input image (I)
Output: Gross Layer (GL), Residual Layer (RL) and Fine Layer (FL)

---

1. Convolve input image (I) of size M×N with cardinal and sub-cardinal directional matrices to obtain composite coefficient (CC) as follows along the respective directions to acquire respective textural details using equation (1):-

$$\left.\begin{array}{c} CC_{north} = \sum_{i=0}^{M}\sum_{j=0}^{N}[I(i,j) \times CD_{north}]\,;\; CC_{south} = \sum_{i=0}^{M}\sum_{j=0}^{N}[I(i,j) \times CD_{south}]\,; \\ CC_{east} = \sum_{i=0}^{M}\sum_{j=0}^{N}[I(i,j) \times CD_{east}]\,;\; CC_{west} = \sum_{i=0}^{M}\sum_{j=0}^{N}[I(i,j) \times CD_{west}]\,; \\ CC_{north-east} = \sum_{i=0}^{M}\sum_{j=0}^{N}[I(i,j) \times SCD_{north-east}]\,;\; CC_{north-west} = \sum_{i=0}^{M}\sum_{j=0}^{N}[I(i,j) \times SCD_{north-west}]; \\ CC_{south-east} = \sum_{i=0}^{M}\sum_{j=0}^{N}[I(i,j) \times SCD_{south-east}]\,;\; CC_{south-west} = \sum_{i=0}^{M}\sum_{j=0}^{N}[I(i,j) \times SCD_{south-west}]\,; \end{array}\right\} \quad (1)$$

where CD_{north} =[0 1 0; 0 -1 0; 0 0 0]; CD_{south} =[0 0 0; 0 -1 0; 0 1 0];
CD_{east} =[0 0 0; 0 -1 1; 0 0 0]; CD_{west} = [0 0 0; 1 −1 0; 0 0 0] ;
$SCD_{north-east}$ =[0 0 1; 0 -1 0; 0 0 0]; $SCD_{north-west}$ = [1 0 0; 0 −1 0; 0 0 0]; $SCD_{south-east}$ =[0 0 0; 0 -1 0; 0 0 1];
$SCD_{south-west}$ =[0 0 0; 0 -1 0; 1 0 0];

2. Obtain a smooth gross image which is referred as GL by low pass filtering operation in the following way as shown in equation (2): -

$$SL = I + \frac{1}{8}[\frac{1}{dy^2}(C_N .* CC_{north} + C_S .* CC_{south}) + \frac{1}{dx^2}(C_E .* CC_{east} + C_W .* CC_{west}) + \frac{1}{dd^2}(C_{NE} .* CC_{north-east} + C_{NW} .* CC_{north-west} + C_{SE} .* CC_{south-east} + C_{SW} .* CC_{south-west}); \quad (2)$$

where $C_N = \frac{1}{\sqrt{1+\frac{CC_{north}}{64}^2}}$, $C_S = \frac{1}{\sqrt{1+\frac{CC_{south}}{64}^2}}$, $C_E = \frac{1}{\sqrt{1+\frac{CC_{east}}{64}^2}}$,
$C_W = \frac{1}{\sqrt{1+\frac{CC_{west}}{64}^2}}$, $C_{NE} = \frac{1}{\sqrt{1+\frac{CC_{north-east}}{64}^2}}$, $C_{NW} = \frac{1}{\sqrt{1+\frac{CC_{north-west}}{64}^2}}$, $C_{SE} = \frac{1}{\sqrt{1+\frac{CC_{south-east}}{64}^2}}$, $C_{SW} = \frac{1}{\sqrt{1+\frac{CC_{south-west}}{64}^2}}$;
$dx^2 = 1, dy^2 = 1, dd^2 = \sqrt{2}$; as *dx* and *dy* denote the respective horizontal and vertical cardinal directional distances along the sinusoidal phase difference of 90◦ while *dd* diagonal distance which is responsible for intermediate direction with sinusoidal phase difference of 45◦ with the current pixel location.

3. RL is obtained as follows as shown in equation (3): -

$$RL = I - GL \quad (3)$$

4. FL is estimated by *MACD*. The convergence in MACD means two underlying moving averages of pixel intensities are similar and moving towards each other because of having identical value while divergence means they are drifting apart.

$$FL = MACD(I) \quad (4)$$

where $MACD = EMA_{12}(p) - EMA_{26}(p)$ EMA is Exponential Moving Average

EMA_{12} and EMA_{26} represent 12-period (15%) and 26-period (7.5%) EMA of SL with respect to time while the nine-period (20%) EMA of SL the MACD line is used as the signal.

2.2 Fusion of Gross Layers

Fusion of Gross Layers *(GLs)* begins by yielding AM_{GL} by *DSCNN* which acts as a feature extractor to compare the pixel-wise activity levels between corresponding patches of the source image pair estimated from the feature maps generation as in (Mukherjee et al. 2025, Liu et al. 2017). The *AM* and *GLs* are subsequently decomposed employing Laplacian and Gaussian Pyramid respectively for each pyramid is set to the highest possible value $log_2 min\ (M, N)$ while the size of the input image is M×N. The proposed fusion rule is implemented on the decomposed coefficients and further reconstructed to obtain GL_{FUSED} via inverse pyramidal transform. The synthesis of GL_{FUSED} is performed by weighted averaging is imposed while the current pixel location has fair similarity around its neighbours and max-selection rule is implemented whenever the current pixel exhibits lower similarity with its neighbourhood. The pertinent details are described in Algorithm 2.

Algorithm 2: Fusion of *Gross Layers*

Input: Gross Layers (GL_A, GL_B)
Output: Fused Gross Layer (GL_{FUSED})

---

1. Find AM by DSCNN to capture pixel-wise activity differences between complementary information of *GLs*.
2. Decompose AM_{GL} and GLs by employing Laplacian and Gaussian Pyramid respectively for pixel level integration. Hence, the total decomposition level of each pyramid is set to the highest possible value $\lfloor log_2 min\ (M, N) \rfloor$ while the size of the input image is M×N and $\lfloor . \rfloor$ represents flooring operation.
3. Respective *Spatial Energies,* SE_A *and* SE_B of GL_A and GL_B are estimated to incorporate neighbouring influences for l^{th} *level* decomposition, around every pixel location by placing a $m \times n$ sized window as follows in equation (5):-

$$SE^l(i,j) = \sum_{m=-1}^{1} \sum_{n=-1}^{1} L[GL^l(i+m, j+m)]^2 \tag{5}$$

4. *Similarity Measuring coefficient (SMC)* at l^{th} level of decomposition is calculated as shown in equation (6):-

$$SMC^l(i,j) = \frac{2 \sum_{m=-1}^{1} \sum_{n=-1}^{1} [L\{GL_A^l(i+m, j+n)\} \times L\{GL_B^l(i+m, j+n)\}]}{SE_A^l(i,j) + SE_B^l(i,j)} \tag{6}$$

5. GL_{FUSED} at l^{th} level of decomposition by the following decision rule as shown in equation (7):-

$$GL_{FUSED}^l(i,j) = \begin{cases} G\{AM^l(i,j)\} \times L\{GL_A^l(i,j)\} + [1 - G\{AM^l(i,j)\} \times L\{GL_B^l(i,j)\}]; & -1 \le SMC^l(i,j) \le 1 \text{ and } SMC^l(i,j) \ge \tau \\ L\{GL_A^l(i,j)\}; & SMC^l(i,j) < \tau \text{ and } SE_A^l(i,j) \ge SE_B^l(i,j) \\ L\{GL_B^l(i,j)\}; & SMC^l(i,j) < \tau \text{ and } SE_A^l(i,j) < SE_B^l(i,j) \end{cases} \tag{7}$$

where τ stands for *parametric threshold* estimated as global optima by the proposed *WCGWO;*

Weighted averaging type fusion mode is adapted when SMC lies in between the range of -1 to 1 and SMC is bigger than τ as it indicates grater similarity of the current pixel with its neighbouring pixel while for SMC is smaller than τ max-selection rule is applied

6. GL_{FUSED} is ultimately obtained by Laplacian pyramid reconstruction.

2.3 Estimation of Parametric Threshold

The hybridization of WC and GWO is introduced in the present study by mimicking the ranking strategy of teams in terms of *Mean Intensity (μ)* and *Spatial Standard Deviation (SSD)* of the input sub-images used in WC is serving as fitness function in GWO to obtain a reliable and self-characterized τ. GWO is a very popular soft computing approach because hunting strategy of grey wolves associated with attacking the prey in terms of global optima finding procedure is employed with three hierarchical wolves namely α, β, δ (Mirjalili et al.

2014). The position update/step phenomenon of grey wolves are also designed considering Mantegna's algorithm (Yang 2010).

On the other hand, WC is inspired by FIFA world cup competition (Razmjooy et al. 2016) where global optimum is being champion of the league by a country. The score achieved by win, draw and loss are 3, 1 and 0 correspondingly. On the other side, the hierarchy of wolves is found by evaluating their fitness. In this context, *average mean intensity (μ_{avg})* of both modality sub-images and their *spectacular coefficients (s_1 and s_2)* are found from their *spatial standard deviation (SSD)* on the basis of principle eigen value by principle eigen vector which consists of maximum information content which is similar as estimating mean and standard deviation of each continent. The mean and standard deviation of each intensity location with respect to their neighbours is estimated like evaluation of performance of a team with respect to other teams to rank them. The imitation strategy shown in equation (13) is also shown in step 7 of Algorithm 3. This adoption facilitates faster convergence by systematic stepwise reduction of search space. The whole process is elaborated in Algorithm 3.

Algorithm3: Estimation of τ in terms of alphascore by WCGWO

Input: Gross Layers (GL_A, GL_B)
Output: alphascore

---

1. Initialize the grey wolf population and sort the positions in ascending order, X_x, where (x= 1,2,3……..n)
2. The position update phenomenon of grey wolves in search of pray are also designed considering Mantegna's algorithm as shown in equation (9) :-

$$step = \frac{u}{|v|^{\frac{1}{\rho}}};\ \mathrm{u}\sim\mathrm{rand}(0,\sigma_u^2) \text{ and } \mathrm{u}\sim\mathrm{rand}(0,\sigma_v^2);\ \sigma_u = \left\{\frac{\Gamma(1+\rho)\sin(\pi\frac{\rho}{2})}{\Gamma\left[\left(\frac{1+\rho}{2}\right)\rho 2^{(\rho-1)/2}\right]}\right\};\ \rho = \frac{3}{2} \quad (9)$$

where u and v are the normalized random distribution of position of grey wolves while Gamma function is a generalization of the factorial function to non-integer numbers; $\mathrm{stepsize} = 0.001 * \mathrm{step}.*(\mathrm{s} - \mathrm{best})$; s=difference factor; when the solution is the best solution, s remains unchanged; the factor 0.01 comes from the fact that L/100 should be the typical step size of walks/flights and L is the typical length-scale; otherwise, Levy flights may become too aggressive/efficient which makes new solutions (even) jump out side of the design domain and thus wasting evaluations.

3. Now the actual random walks or flights is updated as shown in equation (10) :-

$$\mathrm{s=s+stepsize.*randn(size(s))} \quad (10)$$

where s is constrained as s=s.*(~(Flag4ub+Flag4lb))+ub.*Flag4ub+lb.*Flag4lb;

while upper bound is restricted by:-

Flag4ub=s>ub; $ub = \sqrt{EN^2 + SD^2 + SF^2}$ and Flag4lb=s<lb; $lb = -ub$

4. Find SD_A and SD_B from GL_A and GL_B correspondingly to estimate the pair-wise match outcome as follows shown in equation (11):-

$$SSD(i,j) = \sum_{m=-1}^{1}\sum_{n=-1}^{1}[I\,(i+m\,,j+n) - \mu_n] \quad (11)$$

Where $SD(i,j) > 0$ means performance of spatial location *(i,j)* is better than μ_n for minimization, where *(i,j)* and μ_n are assumed as a team compared with average performance of other participating team in FIFA world cup, which is similar as μ_n represents mean intensity around eight neighboring pixels

5. Compute the covariance of SSD_A and SSD_B for estimating the eigen vectors and eigen values in descending order.
6. Find s_1 and s_2 by choosing the principle eigen vectors (E_{SSDA} and E_{SSDB}) having the highest eigen value which signifies the maximum information content as follows described by equation (12): -

$$s_1 = \frac{E_{SSDA}}{E_{SSDA}+E_{SSDB}};\ s_2 = \frac{E_{SSDB}}{E_{SSDA}+E_{SSDB}} \quad (12)$$

7. The fitness function is characterized as shown in equation (13): -

$$fitness = (m_1 \times s_1 + m_2 \times s_2) + \mu_{avg} \quad (13)$$

Where s_1 and s_2 are assumed as two competing teams; while m_1 and m_2 are small draw tolerances between s_1 and s_2 are calculated in similar way; for the match points awarded to s_1 with respect to s_2 (m_1)

$$m_1 = \begin{cases} 3, & if\ s_1 > s_2;\ \ when\ s_1\ wins\ due\ to\ having\ grater\ information\ content \\ 1, & if\ s_1 = s_2;\ \ when\ match\ \ draw\ between\ s_1\ and\ s_2 \\ 0; & if\ s_1 < s_2;\ \ when\ \ (i,j)\ \ loses \end{cases} \quad (14)$$

8. Calculate the fitness of each sample and rank the wolves in descending order on the basis of fitness value as:-

$$X_\alpha = \ the\ best\ search\ agent$$
$$X_\beta = \ the\ second\ best\ search\ agent$$
$$X_\delta = \ the\ third\ best\ search\ agent$$

9. Absolute Goal Difference ($|GD|$) is analogue as the sum of pair-wise fitness margin is defined as:-

$$|GD|_t(i,j) = \sum_{SSD(i,j)\neq\mu_n} |SSD(i,j) - \mu_n| \quad (15)$$

10. Tie occurs when $SSD(i,j) = \mu_n$; for minimization large positive signed GD or smaller $|GD|$ is preferred depending upon problem definition. In the present context *inverted signed GD (GD*)* signifies favoring wolves having better knowledge about the position of prey.

$$|GD^*|_t(i,j) = -\sum_{SSD(i,j)\neq\mu_n} |\mu_n - SSD(i,j)| = (\text{Rb-1})\, SSD_t(i,j) - \mu_n \quad (16)$$

Maximum possible points per round-robin: 3(Rb-1); due to three hierarchical leader each of them had to compete with other two wolves

11. Sort m1, m2 and $|GD^*|$ in descending order to find respective weight factors namely $\omega_\alpha, \omega_\beta, \omega_\delta$.
12. while (current iteration<t)

for each search agent update the position of wolves mimicking the SOL as :-

$$\overrightarrow{X_\alpha^*} = \overrightarrow{X_\alpha} + \overrightarrow{C_1} * \overrightarrow{r_1}(\overrightarrow{X_\alpha} - \vec{X}), \overrightarrow{X_\beta^*} = \overrightarrow{X_\beta} + \overrightarrow{C_2} * \overrightarrow{r_2}(\overrightarrow{X_\beta} - \vec{X}), \overrightarrow{X_\delta^*} = \overrightarrow{X_\delta} + \overrightarrow{C_3} * \overrightarrow{r_3}(\overrightarrow{X_\delta} - \vec{X}) \quad (17)$$

where *champion team*, *runner up*, *third position obtaining team* are as α, β, δ while *X is any random wolf of the whole pack* like *R1* in *SOL*

$$\overrightarrow{X^*}(t+1) = \frac{(\omega_\alpha \times \overrightarrow{X_\alpha^*} + \omega_\beta \times \overrightarrow{X_\beta^*} + \omega_\delta \times \overrightarrow{X_\delta^*})}{\omega_\alpha + \omega_\beta + \omega_\delta} \quad (18)$$

$$\overrightarrow{X^*}(t+1) = \overrightarrow{X^*}(t+1) + s$$

end for

6. Update *α, A and C*
7. Calculate the fitness of all wolves and update the position as shown in step 5 to converge

t=t+1

end while

8. Return updated $\overrightarrow{X_\alpha^*}$ as alphascore

2.4 Evaluation of the proposed WCGWO hybridization

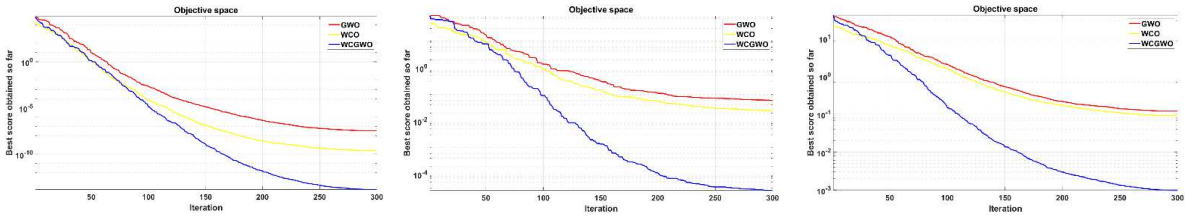
The convergence characteristics of the *WCGWO* is evaluated of the proposed algorithm with the present parameter settings and also compared with two selected benchmark functions like one unimodal (f_1) and multimodal (f_4) as stated in CEC 2022 (Nadimi et al. 2021). One of the unimodal test functions is chosen to analyse its suitability in the exploitation phase to find the optimal solution. On another side, the competency in the exploration phase and the capacity of avoiding the possibility of getting stuck at the local optima is tested via multimodal functions. The changing positions/best score with the iterations is illustrated in Fig. 2. The mathematical representations of the selected test functions are depicted in Table1.

Table1: Benchmark functions

Type of function	Function details	Range
Unimodal	$f_1(x) = \sum_{i=1}^{n} \lvert x_i \rvert^2$	[-100 100]

Multimodal	$f_4(x) = max_i\{\|x_i\|, 1 \le i \le n\}$	[-100 100]
Proposed	$f(GL) = \frac{S_1 \times S_2}{2} + \mu_{avg}$	$\sqrt{EN^2 + SD^2 + SF^2}$

The change of positions/best score is very abrupt during the initial stages which signify the random movements of the whole pack to track the prey in the exploration phase and gradually reduces to emphasize on the exploitation phase to reach to the point of convergence as desired. The implementation of the proposed fitness function in the designed model shows its efficiency in finding the optimum solution in both stages of exploration and exploitation. The faster convergence capability of the proposed hybridized WCGWO algorithm than that of GWO and WC individually is demonstrated by Fig.2.



(a) f_1 (b) f_4 (c) proposed

Fig. 2: Convergence characteristics of GWO and the proposed hybridized WCGWO algorithm

2.5 Fusion of Residual Layers

Prior to fusion, *Cloud Coefficents (CC_A and CC_{RB})* are derived from the respective RL_A and RL_B via *SCM* by (Li et al. 2018) which predicts randomness and fuzziness by estimating statistical properties including *expectation (EXP), entropy (EN), and hyper-entropy (HE)*. HE is signifying the thickness of the cloud and it is determined by the root mean square summation of EN and *Standard Deviation (SD)*. EXP represents the certainty of a qualitative concept, revealing the average level of brightness. EN quantifies the uncertainty of the qualitative concept, providing a measure of randomness and fuzziness by estimating the degree of dispersion of cloud droplets. The schematic representation is demonstrated in Fig. 3.

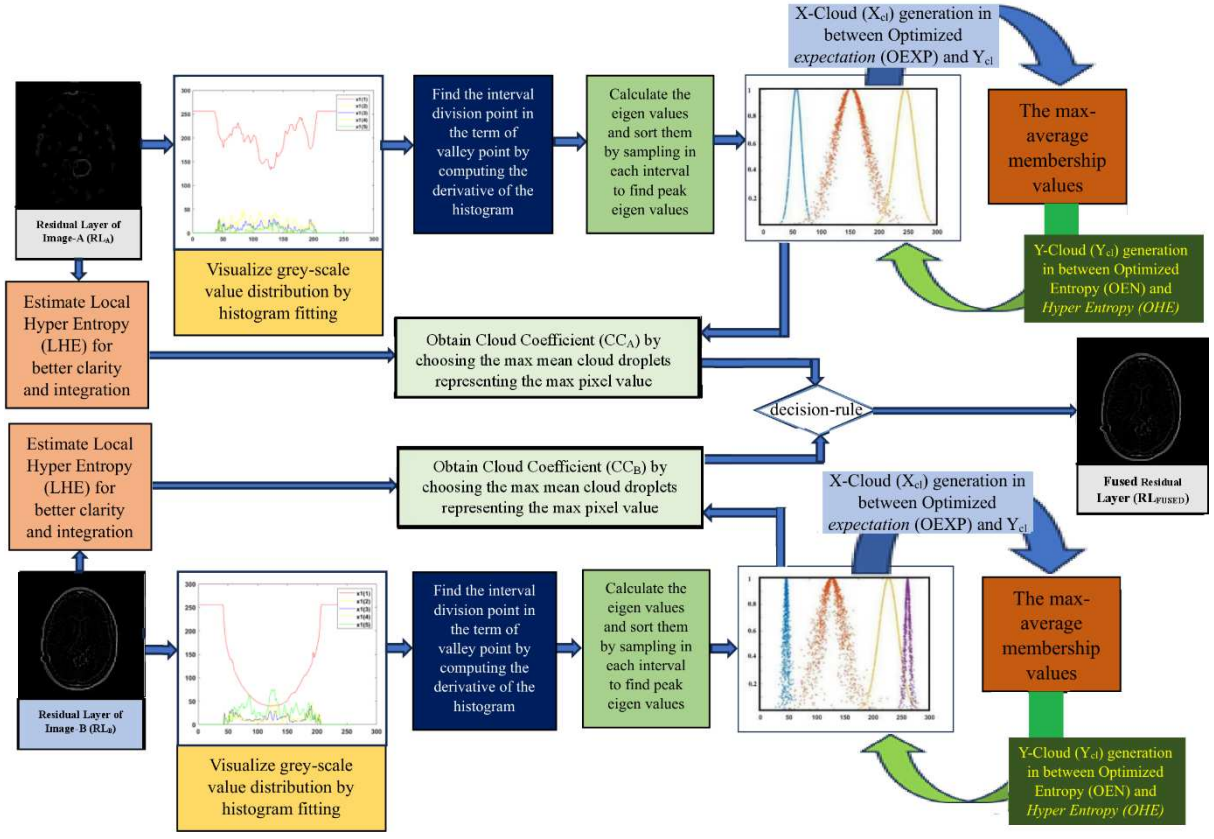


Fig. 3: Schematic representation of estimating *Fused Residual Layer (RL_{FUSED})* through *Statistical Cloud Model (SCM)*

Fusion of *Residual Layers* is performed by estimating the static property of the input image only. Hence it is named so. On the other hand, X-cloud (X_{cl}) and Y-cloud (Y_{cl}) are produced in the range of random distribution between *Entropy (EN)* and *Hyper Entropy (HE)*. The whole process aims to enhance clarity and better information integration and is elaborated in Algorithm 4.

Algorithm 4: Fusion of Residual Layers by estimating Cloud Coefficients (CC)

Input: Residual Layers (RL_A, RL_B)
Output: Fused Residual Layer (RL_{FUSED})

---

1. Fit the histogram of *I* to obtain the fitted curve.
2. Compute the derivative function of the fitted curve to find an appropriate valley point which is the symbol of interval divide.
3. Calculate the eigenvalues.
4. Sort the eigen values by sampling in each interval; which is known as multistep backward cloud transformation algorithm. It is based on the sample division to find the peak eigen values successively for reducing redundancy.
5. The *spatial entropy (SEN), spatial hyper entropy (SHE)* are estimated like *SSD* as shown in step 4 of algorithm 3 by placing 3×3 sliding window to acquire regional features. The estimations are performed as follows in equation (16):-

$$SEN[I(i,j)] = -\frac{1}{m\times n}\sum_{m=-1}^{1}\sum_{n=-1}^{1} P[I(i+m,j+m)] \times log_2 P[I(i+m,j+n)];\ SHE = \sqrt{SEN^2 + SSD^2} \quad (16)$$

where *P[I(i+m,j+n)]* is the probability of occurrence of *I(i+m,j+n)*;

6. Generate *Y-clouds (Y_{cl})* and *X-clouds (X_{cl})* using *forward cloud model* as follows in equation (17)-

$$Ycl = rand(EN, HE);\ Xcl = rand(EXP, Ycl) \quad (17)$$

7. The *cloud drops* are CD_R which is generated as shown in equation (18)-

$$CD_R(i,j) = \begin{cases} I(i,j); & X_{cl} \geq LHE(i,j) \\ SHE(i,j); & otherwise \end{cases} \quad (18)$$

8. Obtain CD_{RA} *and* CD_{RB} from RL_A and RL_B correspondingly using step 1 to 7.

9. Fusion is performed as shown in equation (19):-

$$RL_{FUSED}(i,j) = \begin{cases} CC_A(i,j); & CD_{RA}(i,j) > CD_{RB}(i,j) \\ CC_B(i,j); & otherwise \end{cases} \quad (19)$$

2.6 Fusion of Fine Layers

The comprehensive information of the FLs is fed to the SAPCNS. The SAPCNS consists of three data units: *Feeding Input (FI)*, *Linking Input (LI)*, and *Dynamic Threshold unit (D_τ)*, along with a finite set of *Spiking Rules (SR)*. The coupled *neuron (δ)* is the function of input parameters expressed as follows:

$$\delta(i,j) = f\{FD(i,j), LI(i,j), \mathrm{D}_\tau(i,j), SR(i,j)\} \quad (20)$$

Where $SR(i,j) = \lim_{a^{FD}, a^{LI}, a^{D_\tau} \to \rho} \frac{\varepsilon}{f(a^{FD}, a^{LI}, a^{D_\tau})}$; and $\rho \geq 0;\ D_\tau \geq 0;$

While firing condition, $\varepsilon \equiv ((n_t(i,j) \geq D_{\tau_t}(i,j)) * (\mathrm{FD}_t(\mathrm{i,j}) \geq \mathrm{FD}_t) * (\mathrm{LI}_t(\mathrm{i,j}) \geq \mathrm{LI}_t) * (\mathrm{D}_\tau(i,j) \geq \mathrm{D}_\tau)$ and

$$n(\mathrm{i,j}) = FD(\mathrm{i,j})\{1 + LI(i,j)\}$$

When the firing condition is satisfied, the *neuron (δ)* at (i,j)-th spatial location fires, and the state update equation are hence characterized as

$$FD_{t+1}(i,j) = \begin{cases} FD_t(i,j) - FD(i,j) + ES(i,j) + \sum_{\delta_{kl} \leftarrow \sigma_r} \rho_{kl} \omega_{kl_t}; & \delta(i,j) > \varepsilon \\ FD_t(i,j) + ES(i,j) + \sum_{\delta_{kl} \leftarrow \sigma_r} \rho_{kl} \omega_{kl_t}; & otherwise \end{cases} \quad \ldots\ldots\ldots\ldots\ldots\ldots(28)$$

$$LI_{t+1}(i,j) = \begin{cases} LI_t(i,j) - LI + ES(i,j) + \sum_{\delta_{kl} \leftarrow \sigma_r} \rho_{kl} \omega_{kl_t}; & \delta(i,j) > \varepsilon \\ LI_t(i,j) + ES(i,j) + \sum_{\delta_{kl} \leftarrow \sigma_r} \rho_{kl} \omega_{kl_t}; & otherwise \end{cases} \quad \ldots\ldots\ldots\ldots\ldots\ldots(29)$$

$$D\tau_{t+1}(i,j) = \begin{cases} D\tau_t(i,j) - D\tau + \rho; & \delta(i,j) > \varepsilon \\ D\tau_t(i,j); & otherwise \end{cases} \quad \ldots\ldots\ldots\ldots\ldots\ldots(30)$$

where *External Stimulus (ES)* of SAPCNS is fed to *FD* to initialize the model, ρ_{kl} denotes the value of spikes received by $\delta(i,j)$; while $\sigma_r\{\delta(i,j)\} = \{\delta_{kl} | k - i| \leq r, |l - j| \leq r\}$

The basic architecture of SAPCNS is exactly same as (Peng and Wang 2018). But the parameter settings are designed by characterizing the properties of the FL-images. The detailed parameter setting along with fusion is described in Algorithm 5.

Algorithm 5: Fusion of Fine Layers by estimating Integrated Activity Level

---

Input: Fine Layers (FL_A, FL_B)
Output: Fused Fine Layer (FL_{FUSED})

---

1. Compute *Spatial gradient energy (SGE)* and *Gradient Window (GW)* is estimated by eqs.(31) and (32) respectively by placing a 3× 3 sliding window around every pixel location as follows-

$$SGE(i,j) = \sum_{m=-1}^{1} \sum_{n=-1}^{1} [FL\,(i+m\,, j+n)]^2 \times W \ldots\ldots\ldots\ldots\ldots\ldots\ldots\ldots\ldots\ldots(31)$$

$$GW(i,j) = \sum_{m=-1}^{1} \sum_{n=-1}^{1} [SGE\,(i+m\,, j+n)]^2 \times W \ldots\ldots\ldots\ldots\ldots\ldots\ldots\ldots\ldots\ldots(32)$$

where $W = 1/16(1\ 2\ 1;\ 2\ 4\ 2;\ 1\ 2\ 1)$;

$$RGO(i,j) = |\sum_{m=-1}^{1} \sum_{n=-1}^{1} [FL(i,j) - FL(i+m\,, j+n)]^2 * w(m,n)|; \ldots\ldots\ldots\ldots\ldots(33)$$

Where $w = \begin{cases} \frac{1}{\|(i,j)-(m,n)\|}; & i,j \neq m,n \\ 0 \quad\quad\quad ; & i,j = mn \end{cases}$

2. Characterize *External Stimulus (ES)* is shown in equation (34); by finding weighted averaging of *SGE and GW* through computing and selecting the eigenvectors corresponding to the highest eigenvalues, which represent the maximum information content and arranged in descending order as-

$$ES = w_{SGE} \times SGE + w_{GW} \times GW \ldots\ldots\ldots\ldots\ldots\ldots\ldots\ldots\ldots\ldots(34)$$

where $w_{SGE} = \frac{E_{SGE}}{E_{SGE}+E_{GW}}$; $w_{GW} = \frac{E_{GW}}{E_{SGE}+E_{GW}}$; E_{SGE} and E_{GW} are eigen vectors estimated from *SGE* and *GW* respectively

3. Obtain the *Fired times* (F_τ) by feeding *Dynamic threshold* (D_τ), initial threshold, τ_0 =1, local weight matrix(ω_L), which is the reciprocal of the Euclidean distance, and iteration number, t_{max} = 110 into SAPCNS. There are two firing status either '0' or '1' represent Y_{FR}, is expressed in equation (35) as follows:

$$Y_{FR} = \begin{cases} 1, & F_\tau = max(F_\tau) \\ 0, & otherwise \end{cases} \quad \ldots\ldots\ldots\ldots\ldots\ldots\ldots\ldots(35)$$

4. Obtain the respective firing times (Y_{FRA}, Y_{FRB}) by equation (31) to (35). Then FL_{FUSED} is obtained by:-

$$FL_{FUSED}(i,j) = FL_A(i,j) \times Y_{AFR}(i,j) + FL_B(i,j) \times Y_{BFR}(i,j) \ldots\ldots\ldots\ldots\ldots\ldots\ldots(36)$$

---

3. Experimental Evaluation

3.1 Dataset for validating the efficiency of the proposed fusion scheme:

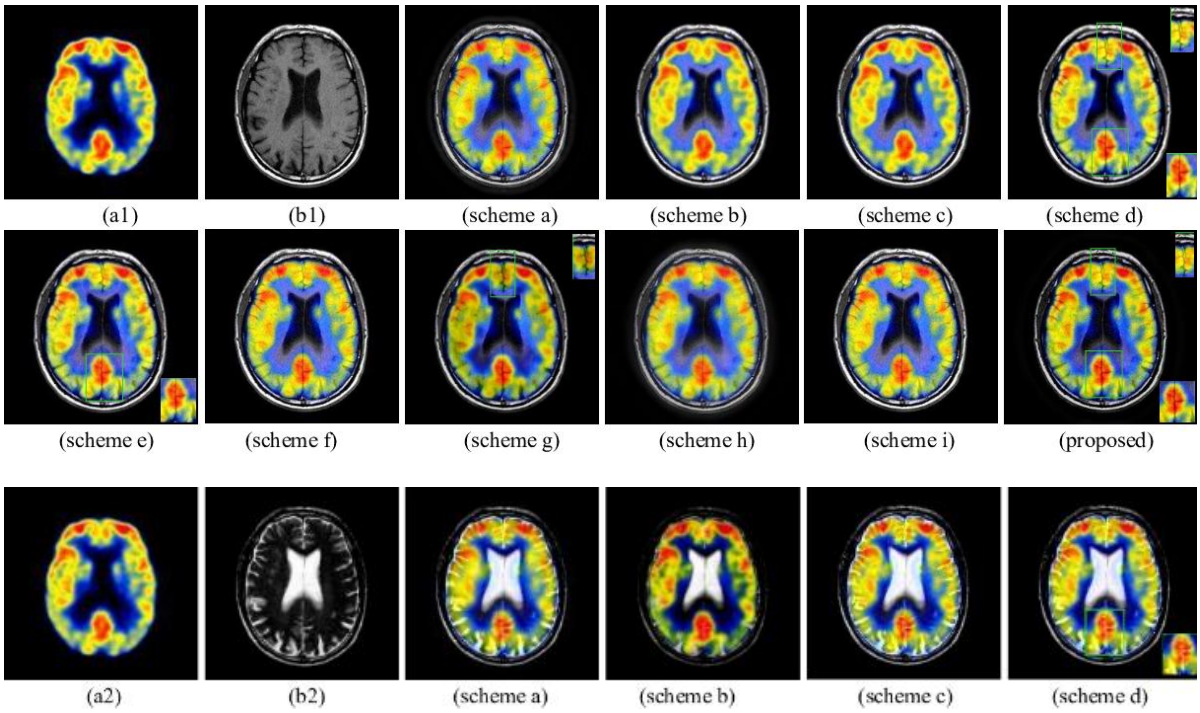
The effectiveness of the proposed method has been validated by applying it on multiple types of brain images, collected from the Whole Brain Atlas (Johnson KA, 2001) by Havard Medical School https://www.med.harvard.edu/aanlib/. The pathological and biographical details of patients are available in the considered database and are presented in Table 2.

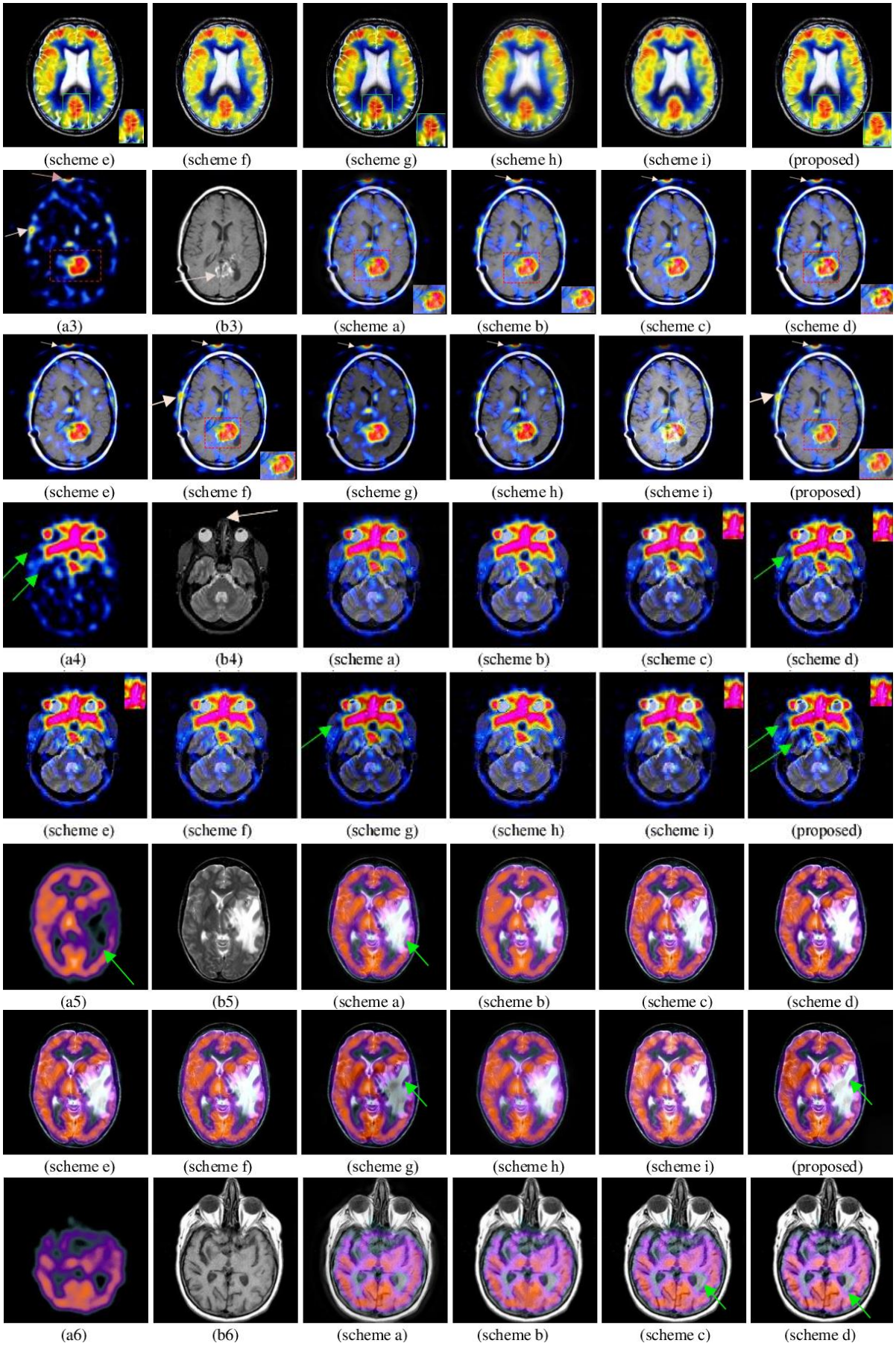
Table 2: Patients' biographical and disease details

Image Set	Age (in years)	Gender	Symptoms	Suspected Cause
S1-S2: I_{A1} to I_{A2} and I_{B1} to I_{B2}	70	Male	Suffering from memory loss about 9 months prior to imaging	abnormality in regional cerebral metabolism due to Alzheimer's disease
S3-S4: I_{A3} to I_{A4} and I_{B3} to I_{B4}	51	Female	Gradual loss of vision and headache	Left frontal astrocytoma
S5: I_{A5} and I_{B5}	42	Female	Memory loss, headache	Brain metastases due to bronchogenic carcinoma
S6-S7: I_{A6} to I_{A7} and I_{B6} to I_{B7}	76	Female	Decline in memory function and processing	Stroke with left hemiparesis Several small deep white and grey matter lesions
S8: I_{A8}-I_{B8}	73	Male	Progressive memory loss	Alzheimer's disease

3.2 Brief overviews of comparative schemes:

The proposed methodology has been compared in this Section with some recent state-of-the-art fusion approaches like (a) Parametrically Optimized PCNN (Mukherjee et al. 2021) (b) max-entropy and regional energy based fusion technique in hybrid decomposition domain (Sharma et al. 2024) (c) extended difference of Gaussian estimation with energy preserving rule (Jie et al. 2023) (d) Fusion considering coupled feature learning via structured convolutional sparse coding mechanism (Veshki et al. 2022) (e) local extreme map guided filtering based fusion (Zhang et al. 2022) (f) truncated Huber-filtering based decomposition with multiple-dictionary learning decisions and nuclear energy associated mechanism (Jie et al. 2024) (g) multi-directional dictionary based complex sparse representation model (Chen et al. 2024) (h) optimal feature selection for medical image fusion using deep learning with transformer (Pathak et al. 2026) (i) residual attention network based fusion (Tang et al. 2025). Fig. 4 demonstrates the fusion images obtained using various methods.




(scheme e)
(scheme f)
(scheme g)
(scheme h)
(scheme i)
(proposed)
(a3)
(b3)
(scheme a)
(scheme b)
(scheme c)
(scheme d)
(scheme e)
(scheme f)
(scheme g)
(scheme h)
(scheme i)
(proposed)
(a4)
(b4)
(scheme a)
(scheme b)
(scheme c)
(scheme d)
(scheme e)
(scheme f)
(scheme g)
(scheme h)
(scheme i)
(proposed)
(a5)
(b5)
(scheme a)
(scheme b)
(scheme c)
(scheme d)
(scheme e)
(scheme f)
(scheme g)
(scheme h)
(scheme i)
(proposed)
(a6)
(b6)
(scheme a)
(scheme b)
(scheme c)
(scheme d)

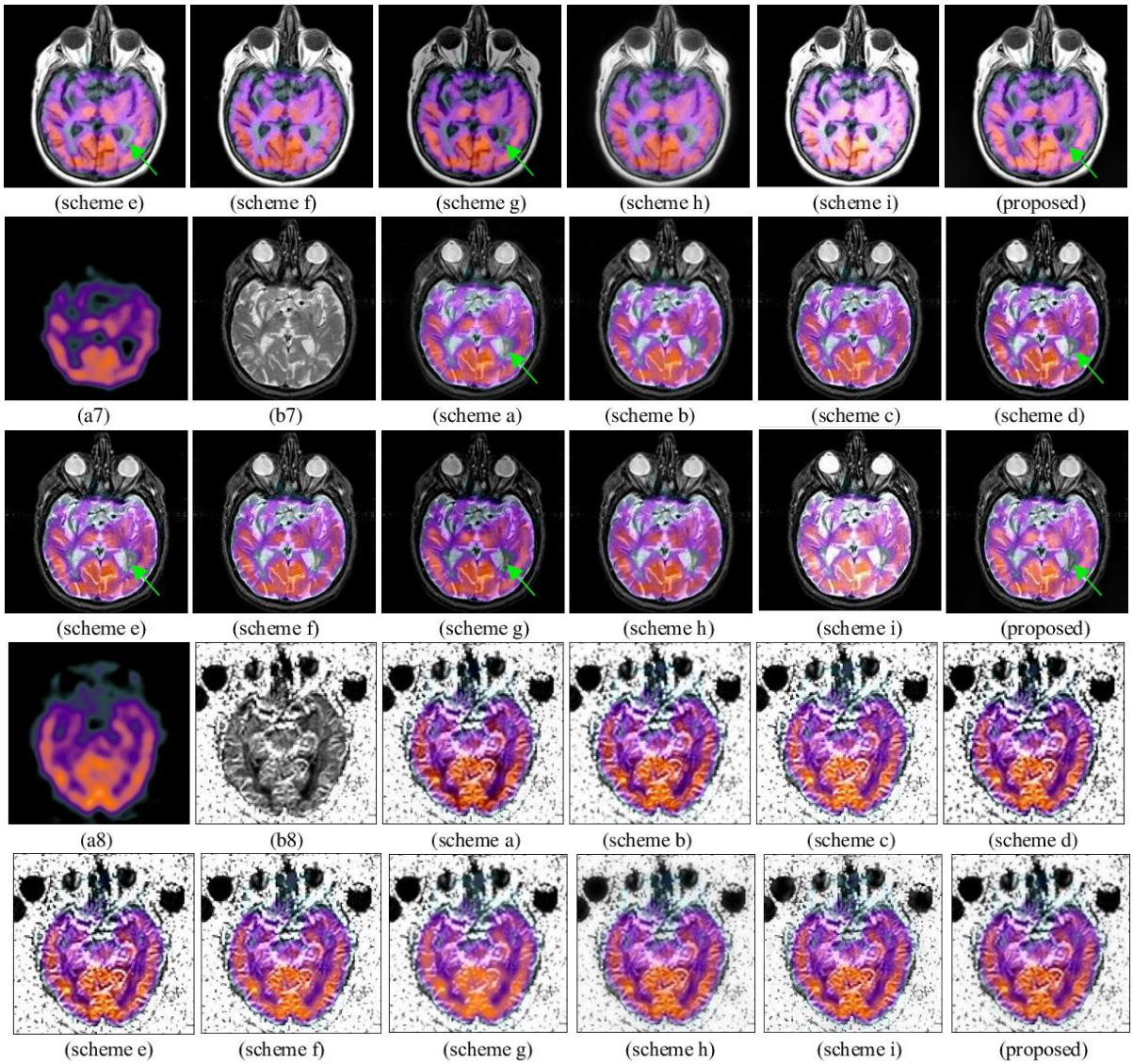


Fig.4: Comprehensive comparative subjective results obtained from multiple fusion schemes

3.3 Subjective Evaluation:

The proposed approach along with the related comparative schemes of eight sets of fusion results are illustrated in fig. 3 that are beneficial to assess visual perceptual quality of the fused images with respect to the source images. The notable preservations achieved by the various schemes are highlighted with distinct markers, and specific significant regions of interest have been included as insets for detailed comparison. Noticeably, for S1 few MRI details are not captured well by the schemes a, b, c; much fairly captured by e, f, g, h, i; while most significantly preserved by d and the proposed method. In case of S2 the gross details are slight blurry by the methods b and i whereas a, c, f capture better and exact retention of the spectacular details are preserved by the schemes d, e, g and proposed very well. The significant edge and color saliency of S3 are visualized noticeably by schemes a, b, d, f and proposed method performs best in capturing every spectacular details. Although, schemes d and g also preserve few significant details of S4 fairly but the proposed method serves best especially retaining the pertinent anatomical and color details of a particular area. The proposed approach along with a, e, g proves their competency by enabling simultaneous visualization of lesion region for S5. The significant saliency acquiring by schemes c, d, e, g are marked by the pointers; scheme g and proposed approach restored MRI details of S6 fairly but proposed one is superior in maintaining good visual clarity. Similarly, for S7 significant edge saliency retention by schemes a, d, e, h and the proposed method is indicated. In case of S8, MRI detailing is slightly blur only by schemes g and rest of methods preserves the requisite details well. According to visual perception it is observed that the proposed technique serves very well in representing relevant edge and color saliency.

3.4 Objective Evaluation:

The effectiveness of the proposed approach has also been verified numerically in terms of some parameters like *EN*, *SD*, *AG, SF*, *NMI* and *TMQI* (Mukherjee et al. 2025) which perform effective evaluation of the information incorporation, visual clarity, representation of finer edges, measurement of activity level, transfer of salient information from the source images, brightness and contrast saliency consecutively. The brief descriptive details of the other parameters are explained as follows:

The parametric indices analyses are the portrayal of effectiveness of various schemes is illustrated in Table 3.

Table 3: Objective assessment of various fusion schemes

Image set	Indices	Various schemes									
		(a)	(b)	(c)	(d)	(e)	(f)	(g)	(h)	(i)	Proposed
S1	EN	5.9106	5.2245	5.0548	4.3692	4.7632	4.9541	4.3271	6.1577	5.3236	**6.1921**
	SD	0.2938	0.3022	0.3119	0.3167	0.3095	0.3126	0.2741	0.2867	0.339	**0.3391**
	AG	0.2638	0.3024	0.2883	0.3369	0.3216	0.3137	0.2871	0.2192	0.2829	**0.3364**
	SF	0.0928	0.1035	0.0943	0.1186	0.1115	0.1115	0.1037	0.0663	0.0884	**0.1327**
	NMI	2.6992	2.7808	3.0176	2.7942	2.8827	3.2404	2.6741	2.6688	2.8094	**3.2437**
	TMQI	0.3732	0.3741	0.3746	0.3755	0.3748	0.3747	0.3712	0.3724	0.3798	**0.3819**
S2	EN	5.3003	4.952	4.7376	3.9593	4.4078	4.7163	4.0507	5.5092	4.667	**5.5791**
	SD	0.3097	0.3183	0.3223	0.3239	0.3181	0.3248	0.2516	0.3081	0.3337	**0.3337**
	AG	0.2481	0.2727	0.2909	0.3018	0.2891	0.2719	0.2798	0.2042	0.2309	**0.3041**
	SF	0.0975	0.1039	0.1111	0.1183	0.1088	0.1072	0.1097	0.0664	0.0704	**0.1394**
	NMI	2.7015	2.7824	3.0121	2.6957	2.7541	3.0255	2.6385	2.7079	2.843	**3.0276**
	TMQI	0.3706	0.3719	0.3724	0.3723	0.372	0.3729	0.3658	0.3704	0.3752	**0.3777**
S3	EN	5.4524	4.9178	4.7666	4.1676	4.2482	4.7119	4.1549	5.7719	5.2062	**5.7909**
	SD	0.2746	0.2734	0.2896	0.2937	0.2877	0.2877	0.2404	0.2647	0.3262	**0.3293**
	AG	0.2121	0.2378	0.2486	0.2628	0.251	0.2466	0.2236	0.1827	0.3619	**0.3702**
	SF	0.0783	0.0974	0.0983	0.1064	0.0991	0.0997	0.0937	0.069	0.1456	**0.1488**
	NMI	2.2203	2.4237	2.5151	2.5405	2.431	2.6189	2.2708	2.2352	2.4156	**2.6249**
	TMQI	0.3639	0.3665	0.3669	0.3661	0.3665	0.3649	0.3679	0.3618	0.3641	**0.3694**
S4	EN	5.1304	5.0884	4.86	4.1489	4.4936	4.8187	4.0391	5.2467	5.0931	**5.3154**
	SD	0.2604	0.256	0.2729	0.2727	0.2683	0.273	0.2791	0.2624	0.2616	**0.2855**
	AG	0.1689	0.1994	0.2069	0.2196	0.2096	0.1974	0.1971	0.1358	0.1804	**0.2366**
	SF	0.0555	0.0683	0.0716	0.0791	0.0737	0.0707	0.0668	0.0412	0.056	**0.095**
	NMI	2.2971	2.3857	2.4806	2.5339	2.551	2.5156	2.4075	2.2102	2.3556	**2.5567**
	TMQI	0.2963	0.2981	0.2985	0.2984	0.2977	0.2976	0.2965	0.2948	0.299	**0.2991**
S5	EN	5.0779	4.7782	4.7549	4.2046	4.4885	4.7234	4.6644	5.1181	4.9703	**5.1185**
	SD	0.3006	0.3064	0.31	0.313	0.3067	0.3072	0.2615	0.3008	0.3333	**0.3346**
	AG	0.1674	0.1643	0.211	0.2232	0.2114	0.1943	0.1956	0.1509	0.2372	**0.2376**
	SF	0.0574	0.0581	0.0743	0.0814	0.0768	0.0699	0.072	0.053	0.0993	**0.0995**
	NMI	2.7312	2.8881	2.81	2.7498	2.7214	2.8571	2.6687	2.8899	2.806	**2.8909**
	TMQI	0.3799	0.3806	0.3801	0.3803	0.3807	0.3805	0.3791	0.3797	0.384	**0.3842**
S6	EN	6.7167	5.9574	5.6802	5.2172	5.4558	5.6779	5.1369	6.8483	3.6759	**6.8515**
	SD	0.315	0.315	0.337	0.3462	0.3387	0.3361	0.2716	0.313	0.3871	**0.3876**
	AG	0.3077	0.3277	0.3698	0.4013	0.3699	0.3654	0.321	0.3081	0.4702	**0.4967**
	SF	0.0879	0.0959	0.1082	0.1186	0.1106	0.1072	0.0983	0.0973	0.1475	**0.1525**
	NMI	2.568	2.6547	2.8559	2.9651	2.9888	3.0297	2.6233	2.5675	2.6513	**3.0298**
	TMQI	0.3925	0.3961	0.3953	0.3942	0.3954	0.3942	0.3964	0.3926	0.4018	**0.4068**
S7	EN	6.2956	6.1922	5.8684	5.0689	5.504	5.8567	4.9776	6.4326	6.0553	**6.4332**
	SD	0.2891	0.2785	0.3015	0.3127	0.3071	0.2993	0.2549	0.2861	0.355	**0.3556**
	AG	0.2883	0.3255	0.3484	0.3719	0.4003	0.3468	0.3105	0.2608	0.4574	**0.4583**
	SF	0.0865	0.1006	0.1052	0.1158	0.1248	0.1047	0.0984	0.0761	0.1535	**0.1563**
	NMI	2.6093	2.7125	2.8512	3.0222	2.8767	2.9314	2.5913	2.5947	2.5983	**3.0346**
	TMQI	0.3673	0.3703	0.3694	0.3707	0.3699	0.3689	0.3678	0.3667	0.3735	**0.3775**
S8	EN	7.3178	6.6892	6.7668	6.2333	5.6123	6.7584	6.9988	7.3972	6.7785	**7.1645**
	SD	0.3225	0.3217	0.3377	0.3586	0.3616	0.3405	0.2606	0.3176	0.3352	**0.3363**
	AG	0.7705	0.6452	0.8349	0.9529	0.9358	0.8226	0.7267	0.7337	0.8495	**0.9543**
	SF	0.2291	0.1953	0.2456	0.269	0.2809	0.2447	0.2105	0.2223	0.2387	**0.2886**
	NMI	2.7191	2.6534	2.9373	2.9278	2.9358	3.0318	2.662	2.7797	2.3669	**3.3944**
	TMQI	0.2704	0.2718	0.2713	0.2695	0.2715	0.2741	0.2361	0.2711	0.257	**0.2812**

Table 3 shows the excellence of the proposed scheme compared to the state-of-the-art techniques in terms of quantitative parameters. The best results are marked in bold to highlight the superiority of the proposed technique. The average score of five parameters is shown in Fig. 4 to demonstrate the effectiveness of the proposed scheme over considered existing methods.

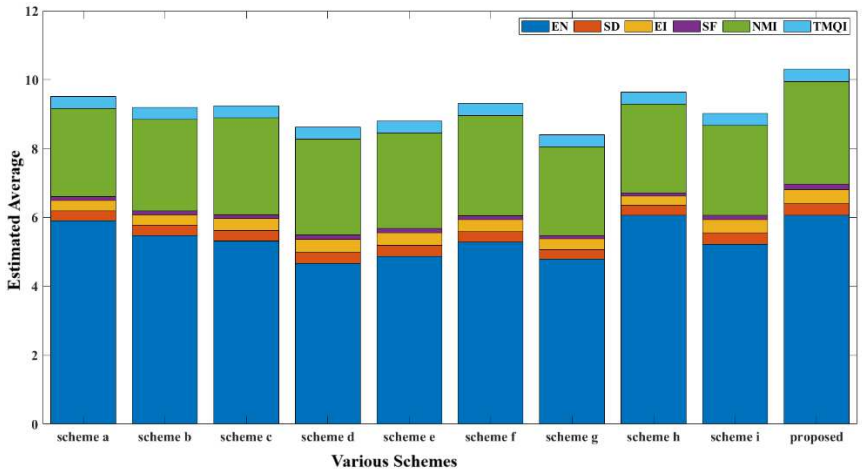


Fig. 5: Average score of selected parameters

The effectiveness of the proposed algorithm is graphically illustrated in Figure 8, demonstrating its ability to manage time complexity and performance efficiency seamlessly. The entire work was conducted using MATLAB 2021a on a system with the following specifications:

- Processor: 11th Gen Intel(R) Core (TM) i3-1125G4 @ 2.00GHz, 2.00 GHz
- RAM: 8 GB (7.75 GB usable)

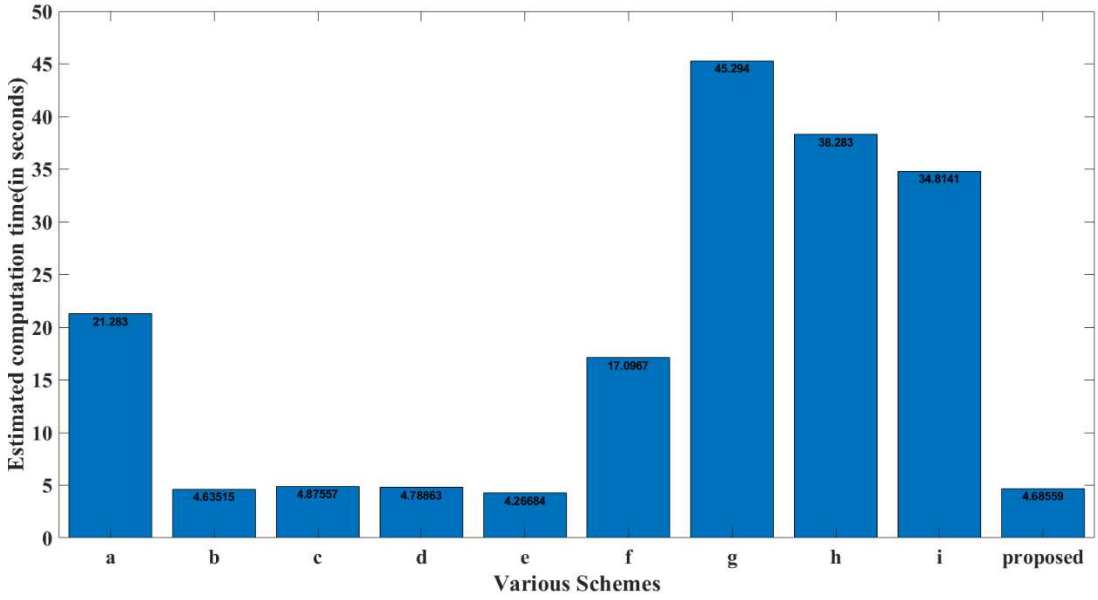


Fig. 8: Time-complexity for executing each algorithm (change)

4. Conclusion and outlook on future scope:

The proposed medical image fusion methodology aims to integrate multimodal complementary images for proper identification and prognosis of brain diseases. In this view, dual stage decomposition is adapted which includes featuring moving average convergence divergence along with cardinal sub-cardinal coordinated filtering and pyramidal decomposition for pixel level context-aware based self-characterized fusion strategy of gross layers along with an automatic threshold detection by the proposed WCGWO with regional property-based combination of residual information by statistical cloud model and pulse coupled neural system also performed well in capturing regional features. The first stage involves local Laplacian and Gaussian pyramidal decomposition for pixel-wise integration of activity map along with parametrical similarity measuring in

accordance with threshold measuring fusion rule of dual decision as a whole substantially improves edge quality especially for max-selection and simultaneous visualization is ensured by weighted averaging in addition to that statistical cloud model also takes care of better information integration and visual clarity of the fused images which is also demonstrated in subjective and objective evaluation. Hence, the proposed method yields superior outcomes and may offer numerous advantages in analyzing diseases as well as to facilitate precise therapy. The proposed decomposition process and hybridization technique might be explored in other fields of image processing in future studies.

Acknowledgment

The authors are grateful to the radiologist Dr. Soumitra Halder from Bankura Sammilani Medical College and Hospital and Dr. Pratip Nandi from R. G. Kar Medical College and Hospitals for providing us their valuable comments on the subjective evaluation of the proposed scheme and the compared state of art approaches.

Funding and/or Conflicts of Interests/Competing Interests Declarations

Conflict of Interest: The authors declare that they have no conflict of interest.
Funding: The authors have not received any funding for this work.

Data Availability Statement

The authors declare that this declaration is not applicable to this research work.

Author's Contribution Declaration

Suranjana Mukherjee- Conceptualization, Data curation, Methodology development, Investigation, Execution, Validation, Original draft preparation.
Sriparna Banerjee- Visualization, Reviewing and Editing
Sheli Sinha Chaudhuri- Supervision
Khalifa Djemal- Supervision

REFERENCES

Basu S, Singhal S, Singh D. A systematic literature review on multimodal medical image fusion. Multimedia tools and applications. 2024 Feb;83(6):15845-913.

Bhosekar S, Singh P, Garg D. A Recent Advancements in Multi-Modal Medical Image Fusion Techniques using SWT, NSST, NSCT, and CNN. In2025 International Conference on Cognitive Computing in Engineering, Communications, Sciences and Biomedical Health Informatics (IC3ECSBHI) 2025 Jan 16 (pp. 928-932). IEEE.

Chen Y, Liu A, Liu Y, He Z, Liu C, Chen X. Multi-dimensional medical image fusion with complex sparse representation. IEEE Transactions on Biomedical Engineering. 2024 Apr 23;71(9):2728-39.

Choudhary G, Sethi D. From conventional approach to machine learning and deep learning approach: an experimental and comprehensive review of image fusion techniques. Archives of Computational Methods in Engineering. 2023 Mar;30(2):1267-304.

Das M, Gupta D, Radeva P, Bakde AM. Optimized multimodal neurological image fusion based on low-rank texture prior decomposition and super-pixel segmentation. IEEE Transactions on Instrumentation and Measurement. 2022 Apr 6;71:1-9.

Dinh PH. Medical image fusion based on enhanced three-layer image decomposition and chameleon swarm algorithm. Biomedical Signal Processing and Control. 2023 Jul 1;84:104740.

Fan C, Yun M, Chen L, Zhao H, Peng B. DWMFusion: A lightweight medical image fusion network based on discrete wavelet convolution and selective state space models. Expert Systems with Applications. 2025 May 8:128040.

Guerroudji MA, Amara K, Lichouri M, Zenati N, Masmoudi M. A 3D visualization-based augmented reality application for brain tumor segmentation. Computer Animation and Virtual Worlds. 2024 Jan;35(1):e2223.

Ghandour C, El-Shafai W, El-Rabaie S, Abdelsalam N. Comprehensive performance analysis of different medical image fusion techniques for accurate healthcare diagnosis applications. Multimedia Tools and Applications. 2024 Mar;83(8):24217-76.

He K, Gong J, Xie L, Zhang X, Xu D. Regions preserving edge enhancement for multisensor-based medical image fusion. IEEE Transactions on Instrumentation and Measurement. 2021 Apr 14;70:1-3.

Ince S, Kunduracioglu I, Algarni A, Bayram B, Pacal I. Deep learning for cerebral vascular occlusion segmentation: a novel ConvNeXtV2 and GRN-integrated U-Net framework for diffusion-weighted imaging. Neuroscience. 2025 May 14;574:42-53.

Jie Y, Li X, Zhou F, Tan H. Medical image fusion based on extended difference-of-Gaussians and edge-preserving. Expert Systems with Applications. 2023 Oct 1;227:120301.

Jie Y, Li X, Tan H, Zhou F, Wang G. Multi-modal medical image fusion via multi-dictionary and truncated Huber filtering. Biomedical Signal Processing and Control. 2024 Feb 1;88:105671.

Johnson KA (2001), The whole brain atlas., Available at https://www.med.harvard.edu/aanlib/home.html

Li M, Jung Y, Fulham M, Kim J. Importance-aware 3d volume visualization for medical content-based image retrieval-a preliminary study. Virtual Reality & Intelligent Hardware. 2024 Feb 1;6(1):71-81.

Li W, Peng X, Fu J, Wang G, Huang Y, Chao F. A multiscale double-branch residual attention network for anatomical–functional medical image fusion. Computers in biology and medicine. 2022 Feb 1;141:105005.

Li W, Du J, Zhao Z, Long J. Fusion of medical sensors using adaptive cloud model in local Laplacian pyramid domain. IEEE Transactions on Biomedical Engineering. 2018 Sep 10;66(4):1172-83.

Liu Y, Chen X, Cheng J, Peng H. A medical image fusion method based on convolutional neural networks. In2017 20th international conference on information fusion (Fusion) 2017 Jul 10 (pp. 1-7). IEEE.

Mirjalili S, Mirjalili SM, Lewis A. Grey wolf optimizer. Advances in engineering software. 2014 Mar 1;69:46-61.

Mukherjee S, Das A. Vague set theory based segmented image fusion technique for analysis of anatomical and functional images. Expert Systems with Applications. 2020 Nov 30;159:113592.

Mukherjee S, Das A. Parametrically Optimized Pulse Coupled Neural Network for Analysis of Multimodal Medical Images. In2021 International Conference on Advances in Electrical, Computing, Communication and Sustainable Technologies (ICAECT) 2021 Feb 19 (pp. 1-6). IEEE.

Mukherjee S, Das A. Relative Global Optimum-Based Measure for Fusion Technique in Shearlet Transform Domain for Prognosis of Alzheimer's Disease. InComputational Intelligence Methods for Super-Resolution in Image Processing Applications 2021 May 29 (pp. 279-291). Cham: Springer International Publishing.

Mukherjee S, Banerjee S, Chaudhuri SS. Hybridized soccer league-grey wolf Optimization algorithm and siamese network synergism based multimodal fusion scheme for prognosis of brain diseases. Multimedia Tools and Applications. 2025 May;84(16):17161-88.

Nadimi-Shahraki MH, Taghian S, Mirjalili S. An improved grey wolf optimizer for solving engineering problems. Expert Systems with Applications. 2021 Mar 15;166:113917.

Pathak DM, Tewari TK, Gupta S, Kalra MK, Saba L, Laine AF, Suri JS. Optimal feature selection for medical image fusion using deep learning with transformer. Biomedical Signal Processing and Control. 2026 Jan 1;111:108377.

Peng H, Wang J. Coupled neural P systems. IEEE Transactions on Neural Networks and Learning Systems. 2018 Oct 23;30(6):1672-82.

Qi B, Li Q, Zhang Y, Zhao Q, Qiao B, Shi J, Lv Z, Li G. Infrared and visible image fusion via sparse representation and adaptive dual-channel PCNN model based on co-occurrence analysis shearlet transform. IEEE Transactions on Instrumentation and Measurement. 2025 Jan 2.

Raju CS, Neelapu BC, Laskar RH, Muhammad G. Analysis of multimodal fusion strategies in deep learning for ischemic stroke lesion segmentation on computed tomography perfusion data. Multimedia Tools and Applications. 2025 Mar;84(10):7493-518.

Razmjooy N, Khalilpour M, Ramezani M. A new meta-heuristic optimization algorithm inspired by FIFA world cup competitions: theory and its application in PID designing for AVR system. Journal of Control, Automation and Electrical Systems. 2016 Aug;27(4):419-40.

Sharma DK, Sachdeva J, Ahuja CK, Singh A. A novel hybrid multimodal medical image fusion scheme based on non-subsampled Shearlet transform. Circuits, Systems, and Signal Processing. 2024 Jun;43(6):3627-48.

Su H, Li Y, Xu Y, Fu X, Liu S. A review of deep-learning-based super-resolution: From methods to applications. Pattern Recognition. 2025 Jan 1;157:110935.

Sun J, Li Y, Wu X, Tang C, Wang S, Zhang Y. HAD-Net: An attention U-based network with hyper-scale shifted aggregating and max-diagonal sampling for medical image segmentation. Computer Vision and Image Understanding. 2024 Dec 1;249:104151.

Tan W, Tiwari P, Pandey HM, Moreira C, Jaiswal AK. Multimodal medical image fusion algorithm in the era of big data. Neural computing and applications. 2020 Jul 8:1-21.

Tang H, Yu L, Shao Y. MARCFusion: adaptive residual cross-domain fusion network for medical image fusion. Multimedia Systems. 2025 Apr;31(2):1-26.

Veshki FG, Vorobyov SA. Coupled feature learning via structured convolutional sparse coding for multimodal image fusion. InICASSP 2022-2022 IEEE International Conference on Acoustics, Speech and Signal Processing (ICASSP) 2022 May 23 (pp. 2500-2504). IEEE.

Wang S, Sun Z, Li Q. High-to-low-level feature matching and complementary information fusion for reference-based image super-resolution. The Visual Computer. 2024 Jan;40(1):99-108.

Xia Q, Zheng H, Zou H, Luo D, Tang H, Li L, Jiang B. A comprehensive review of deep learning for medical image segmentation. Neurocomputing. 2025 Jan 14; 613:128740.

Xu L, Si Y, Jiang S, Sun Y, Ebrahimian H. Medical image fusion using a modified shark smell optimization algorithm and hybrid wavelet-homomorphic filter. Biomedical Signal Processing and Control. 2020 May 1;59:101885.

Yang XS. Nature-inspired metaheuristic algorithms. Luniver press; 2010.

Yin M, Liu X, Liu Y, Chen X. Medical image fusion with parameter-adaptive pulse coupled neural network in nonsubsampled shearlet transform domain. IEEE Transactions on Instrumentation and Measurement. 2018 Jun 14;68(1):49-64.

Zhang Y, Xiang W, Zhang S, Shen J, Wei R, Bai X, Zhang L, Zhang Q. Local extreme map guided multi-modal brain image fusion. Frontiers in Neuroscience. 2022 Oct 28; 16:1055451.

Zhang F, Yang G, Sun J, Wan W, Zhang K. Triple disentangled network with dual attention for remote sensing image fusion. Expert Systems with Applications. 2024 Jul 1; 245:123093.